Impact of mixed anion ordered state on the magnetic ground states of $S = 1/2$ square-lattice quantum spin antiferromagnets, Sr_2NiO_3Cl and Sr_2NiO_3F

Yoshihiro Tsujimoto,[1,2,*] Jun Sugiyama,[3,4] Masayuki Ochi,[5,6] Kazuhiko Kuroki,[5] Pascal Manuel,[7] Dmitry D. Khalyavin,[7] Izumi Umegaki,[8] Martin Månsson,[9] Daniel Andreica,[10] Shigeo Hara,[11] Takahiro Sakurai,[11] Susumu Okubo,[12,13] Hitoshi Ohta,[12,13] Andrew T. Boothroyd,[14] and Kazunari Yamaura[1,2]

[1]*International Center for Materials Nanoarchitechtonics, National Institute for Materials Science, 1-1 Namiki, Tsukuba, Ibaraki 305–0044, Japan*

[2]*Graduate School of Chemical Sciences and Engineering, Hokkaido University, North 13 West 8, Kitaku, Sapporo 060–0808, Japan*

[3]*Neutron Science and Technology Center, Comprehensive Research Organization for Science and Society (CROSS), Tokai, Ibaraki 319–1106, Japan*

[4]*Advanced Science Research Center, Japan Atomic Energy Agency, Tokai, Ibaraki 319–1195, Japan*

[5]*Department of Physics, Osaka University, 1-1 Machikaneyama-cho, Toyonaka, Osaka 560–0043, Japan*

[6]*Forefront Research Center, Osaka University, 1-1 Machikaneyama-cho, Toyonaka, Osaka, 560–0043, Japan*

[7]*ISIS Neutron Facility, Rutherford Appleton Laboratory, Chilton, Ddcot OX11 0QX, United Kingdom*

[8]*High Energy Accelerator Research Organization (KEK), Tokai, Ibaraki 319–1106, Japan*

[9]*Department of Applied Physics, KTH Royal Institute of Technology, Stockholm SE-106 91, Sweden*

[10]*Faculty of Physics, Babes-Bolyai University, 400084, Cluj-Napoca, Romania*

[11]*Research Facility Center for Science and Technology, Kobe University, Kobe 657–8501, Japan*

[12]*Molecular Photoscience Research Center, Kobe University, Kobe 657–8501, Japan*

[13]*Graduate School of Science, Kobe University, Kobe 657–8501, Japan*

[14]*Department of Physics, University of Oxford, Clarendon Laboratory, Oxford OX1 3PU, United Kingdom*

(Received 6 September 2022; revised 24 October 2022; accepted 27 October 2022; published 17 November 2022; corrected 9 December 2022)

The magnetic properties of the $S = 1/2$ two-dimensional square-lattice antiferromagnets Sr_2NiO_3X (X = Cl, F) with the trivalent nickel ions in a low-spin state were studied by magnetic susceptibility, heat capacity, neutron powder diffraction, high-field electron spin resonance (ESR), muon spin rotation and relaxation (μ^+SR) measurements, and density functional theory (DFT) calculations. Both oxyhalides are isostructural to an ideal quantum square-lattice antiferromagnet $Sr_2CuO_2Cl_2$, but the chlorine/fluorine anion exclusively occupies an apical site in an ordered/disordered manner with an oxygen anion, resulting in the formation of highly distorted NiO_5X octahedra with an off-center nickel ion. Magnetic susceptibility measurements revealed a remarkable difference between these two compounds: the magnetic susceptibility of Sr_2NiO_3Cl exhibited a broad maximum at approximately 35 K, which is typical of low-dimensional antiferromagnetic behavior. In contrast, the magnetic susceptibility of Sr_2NiO_3F exhibited spin-glass-like behavior below 12 K. No anomaly associated with long-range magnetic ordering was observed in the heat capacity, ESR, and neutron powder diffraction experiments. However, μ^+SR measurements revealed the emergence of a static magnetic ordered state below T_N= 28 K in Sr_2NiO_3Cl and a short-range magnetic state below T_N= 18 K in Sr_2NiO_3F. The DFT calculations suggested that the unpaired electron occupied a $d_{3z^2-r^2}$ orbital, and ferromagnetic couplings between the nearest-neighbor nickel spins were energetically favored. The mechanism of ferromagnetic superexchange interactions and the reason for the difference between the magnetic ground states in these nickel oxyhalides are discussed.

DOI: 10.1103/PhysRevMaterials.6.114404

I. INTRODUCTION

Low-dimensional quantum spin magnetism is a central subject in condensed-matter physics [1,2]. Among the many types of spin networks, square-lattice Heisenberg antiferromagnets (SLHAFs) have attracted a considerable amount of attention owing to their diverse electronic and magnetic ground states [3,4]. Extensive studies on K_2NiF_4-type oxychlorides $(Sr/Ca)_2CuO_2Cl_2$ (Fig. 1) and related copper oxides with dominant nearest-neighbor (NN) interactions have enriched our understanding of the critical phenomena and phase transitions of SLHAFs and their relationship to superconductivity [5,6].

The development of quantum spin magnetism has led us to search for experimental realization of the frustrated square-lattice Heisenberg antiferromagnet, namely, the $J_1 - J_2$ model, in which the NN interactions (J_1) and the next-nearest neighbor (NNN) interactions (J_2) compete. Theoretical studies on this model predicted unusual quantum spin disordered states: the spin liquid state or valence-bond solid state at $J_2/J_1(= \alpha) \approx 0.4$–$0.6$, and the spin nematic state in

*Corresponding author: TSUJIMOTO.Yoshihiro@nims.go.jp

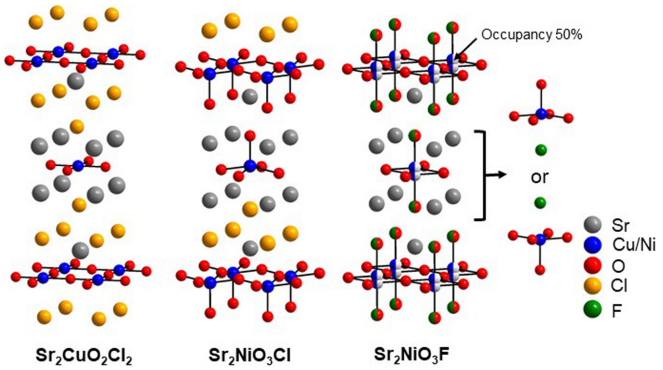

FIG. 1. Crystal structures of Sr_2CuO_2Cl, Sr_2NiO_3Cl, and Sr_2NiO_3F. The halide ions exclusively occupy apical anion sites with Cl/F anions being ordered/disordered. The Ni cation, which is off-centered owing to the different bonding nature against oxygen and halogen, forms square pyramidal coordination with oxygen anions.

the vicinity of $\alpha \approx -0.5$ [7–12]. $PbVO_3$ with a $PbTiO_3$-type structure, which may be placed at approximately $0.2 < \alpha < 0.4$, exhibits no long-range magnetic order down to low temperatures and is a good candidate for the square-lattice J_1–J_2 model with a quantum spin disordered state [13], [14]. Moreover, it has been reported that the double perovskite oxide $Sr_2Cu(Te_{1-x}W_x)O_6$, with random magnitudes of J_1 and J_2, exhibits gapless spin-liquid-like behavior at the phase boundary between the Néel -type order ($x = 0$) and the columnar order ($x = 1$) [15–17]. A recent theoretical work by Uematsu and Kawamura suggested the existence of a random-singlet state, analogous to the quantum spin-liquid state in Kagome and triangular lattice antiferromagnets [18].

Sr_2NiO_3Cl and Sr_2NiO_3F, which crystallize in a K_2NiF_4-type structure, are rare SLHAFs consisting of Ni^{3+} in the low-spin state (i.e., $S = 1/2$) [19]. As shown in Table I, unlike Sr_2CuO_2Cl with flat CuO_2 sheets sandwiched between chloride ions, nickel oxyhalides have a corrugated NiO_2 plane at O_{eq}–Ni–O_{eq} bond angles of approximately 165° owing to the occupation of either apical site by a halide ion to form highly distorted octahedra $NiO_5(Cl/F)$. Given that these halide ions are located at a longer distance than expected from the ionic radii [20], the nickel centers can be viewed as pseudosquare pyramids NiO_5. Furthermore, the apical halogen sites are ordered in Sr_2NiO_3Cl and disordered in Sr_2NiO_3F, which appears to be correlated with their magnetic ground states, namely an antiferromagnetic phase transition at 33 K in Sr_2NiO_3Cl and a spin-glass-like transition at 11 K in Sr_2NiO_3F, as suggested by magnetic susceptibility measurements from a previous study [19]. However, the underlying magnetism remains to be elucidated. The Curie-Weiss fit indicated the presence of dominant ferromagnetic interactions in both oxyhalides (Weiss temperature: 24.2 K for Sr_2NiO_3Cl and 21.3 K for Sr_2NiO_3F), which is not typical of K_2NiF_4-type compounds. One exception is copper-based fluorides A_2BF_4 (A = K, Rb, Cs; B = Cu, Ag), which exhibit a ferromagnetic phase transition at low temperatures [21–24]. The ferromagnetism is related to the alternating arrangement of Cu/Ag $d_{x^2-z^2}$ and $d_{y^2-z^2}$ orbitals in the ab plane [25–28]. Clearly, this is not the case with the current nickel oxyhalides. In a previous study, we proposed that a single unpaired electron occupies the d_{xy} orbital pointing in the diagonal direction leading to dominant ferromagnetic interactions between the NNN nickel ions [19]. Whether the NNN interaction is ferromagnetic or antiferromagnetic, however, it is unlikely that in the K_2NiF_4-type structure, it is greater than the NN interaction. In addition, although spin frustration is a typical ingredient of spin-glass behavior, this state does not appear in the proposed $J_1 - J_2$ model. To better understand the magnetic ground states of Sr_2NiO_3Cl and Sr_2NiO_3F, we investigated their physical properties using magnetic susceptibility, heat capacity, neutron powder diffraction, muon spin relaxation and rotation measurements, and first-principles calculations.

TABLE I. Selected bond lengths and bond angles in Sr_2NiO_3Cl and Sr_2NiO_3F.

Sr_2NiO_3Cl		Sr_2NiO_3F	
Ni–O_{eq}	1.9417(9) Å	Ni–O_{eq}	1.900(1) Å
Ni–O_{ap}	1.904(5) Å	Ni–O_{ap}/F	2.013(8) Å
Ni–F	3.099(9) Å		2.483(8) Å
$\angle O_{eq}$–Ni–O_{eq}	162.7(4)°	$\angle O_{eq}$–Ni–O_{eq}	165.8(4)°

II. EXPERIMENTAL

Polycrystalline Sr_2NiO_3Cl and Sr_2NiO_3F samples were synthesized using a high-pressure and high-temperature method. In an earlier report, SrO_2, $SrCl_2$, SrF_2, and Ni were used as the starting materials [19]. However, it was challenging to obtain both nickel oxyhalides as a homogeneous phase under the previously reported reaction conditions, which is probably owing to the coarse particle size of the nickel powder used. NiO was utilized as an alternative Ni source to facilitate the reaction. A stoichiometric mixture of in-house synthesized SrO_2, SrO (obtained by heating $SrCO_3$ at 1300 °C in O_2 flowing atmosphere), NiO (3N, High Purity Materials), $SrCl_2$ (3N, Rare Metallic), and SrF_2 (3N, Rare Metallic) was finely ground in an agate mortar in an Ar-filled glovebox, loaded into a Pt capsule, and heated in a belt-type high-pressure apparatus for 1 h at 3 GPa and 1500 °C for Sr_2NiO_3Cl and for 1 h at 6 GPa and 1500 °C for Sr_2NiO_3F. The sample was then quenched to room temperature by turning off the heater, and the pressure was slowly released. The sample quality was assessed using laboratory powder x-ray diffraction (XRD) analysis.

The magnetic susceptibilities of Sr_2NiO_3Cl and Sr_2NiO_3F were measured over the temperature range of T = 2–350 K at various magnetic fields using a superconducting quantum interference device magnetometer (Quantum Design, MPMS-XL). The heat capacity under a zero magnetic field was recorded between 3 and 250 K on cooling by a pulse relaxation method using a commercial calorimeter (Quantum Design PPMS).

Neutron powder diffraction (NPD) data were collected for Sr_2NiO_3Cl and Sr_2NiO_3F at various temperatures using the WISH diffractometer located at the second target station at the ISIS pulsed neutron source in the UK [29]. The NPD data were analyzed by the Rietveld method using the FULLPROF program [30].

High-field ESR measurements of the Sr_2NiO_3Cl powder samples were performed using pulsed magnetic fields and transmission methods. Gunn oscillators were used as the light sources. The temperature range measured was between 1.9 and 265 K. Lower temperatures than the boiling point of liquid helium were obtained by pumping helium. By flowing nitrogen gas, temperatures higher than those of liquid nitrogen were obtained. The experimental details are available in Refs. [30–32].

Muon spin rotation and relaxation (μ^+SR) measurements were performed on the Multi-Purpose Surface-Muon Instrument (Dolly) spectrometer at the surface muon beamline piE1 of the Laboratory for Muon Spin Spectroscopy (LMU) of the Paul Scherrer Institute (PSI) in Switzerland. The μ^+SR spectra were recorded in zero magnetic field (ZF), transverse field (TF), and longitudinal field (LF). Here, TF/LF is the magnetic field perpendicular/parallel to the initial muon spin polarization. The details of the setup and experimental procedure for the μ^+SR experiments are described elsewhere [34], [35]. The obtained μ^+SR spectra were analyzed using MUSRFIT [36].

First-principles calculations based on DFT theory were performed using the WIEN2K software [37,38]. The experimental crystal structure of Sr_2NiO_3Cl was used in the calculations [19]. The generalized gradient approximation with the Perdew-Burke-Ernzerhof parameterization [39] was used with the Hubbard U correction of the fully localized limit version, also known as the self-interaction correction [40,41]. We used $U = 4$ eV and verified that other U values did not alter our calculation results qualitatively. The muffin-tin radii of atoms are 2.33, 1.92, 1.65, 2.5 Bohr for Sr, Ni, O, Cl atoms, respectively. The $RK_{\max}$ parameter was set to 7, which is a product of the shortest muffin-tin radius of an atom (1.65 Bohr in our case) and the plane-wave cutoff. The maximum value of l (azimuthal quantum number) for partial waves used in the computation of non-muffin-tin matrix elements was set to 6. We used a conventional rectangular unit cell including two Ni atoms or a $\sqrt{2} \times \sqrt{2} \times 1$ supercell depending on the periodicity of the magnetic states. We used an $11 \times 11 \times 3$ k-mesh for the conventional unit cell and a $7 \times 7 \times 3$ k-mesh for the supercell. We used a $21 \times 21 \times 5$ k-mesh for calculating the density of states (DOS).

III. RESULTS

A. Powder neutron diffraction

The NPD data collected from Sr_2NiO_3Cl and Sr_2NiO_3F can be readily indexed to the tetragonal space groups $P4/nmm$ and $I4/mmm$, respectively, confirming the order of Cl atom and disorder of F atom in the lattice. In the case of $I4/mmm$ symmetry, Ni is disordered over the 4e Wyckoff positions in correlation with the random distribution of F atoms in the apical sites of coordination octahedra. The calculated lattice constants at 4 K are $a = 3.83920(4)$ Å and $c = 14.3638(3)$ Å for Sr_2NiO_3Cl and $a = 3.77082(1)$ Å and $c = 13.0617(3)$ Å for Sr_2NiO_3F. These values are consistent with those from a previous study, with the exception that the volume of both cells decreases upon cooling [19]. At low temperatures, neither of the compounds displayed any additional peaks or extra intensity increase associated with magnetic ordering, which implies the presence of strong quantum fluctuations (See the Supplemental Material [42] for the neutron powder diffraction data of Sr_2NiO_3Cl at 1.5 and 30 K). Figure 2 shows the results of Rietveld refinement against the 1.5 K NPD data. The final refined crystallographic data summarized in Table II are consistent with those obtained from room-temperature synchrotron XRD data [19], with the exception of the detection of 3% oxygen vacancies at the equatorial sites in Sr_2NiO_3F. NiO and the uncharacterized peaks were detected as minor phases as well. Upon refinement, the mass fractions of NiO were estimated to be 1.7% for Sr_2NiO_3Cl and 5.2% for Sr_2NiO_3F. Such a minute quantity of impurities would not hinder the evaluation of the intrinsic physical properties.

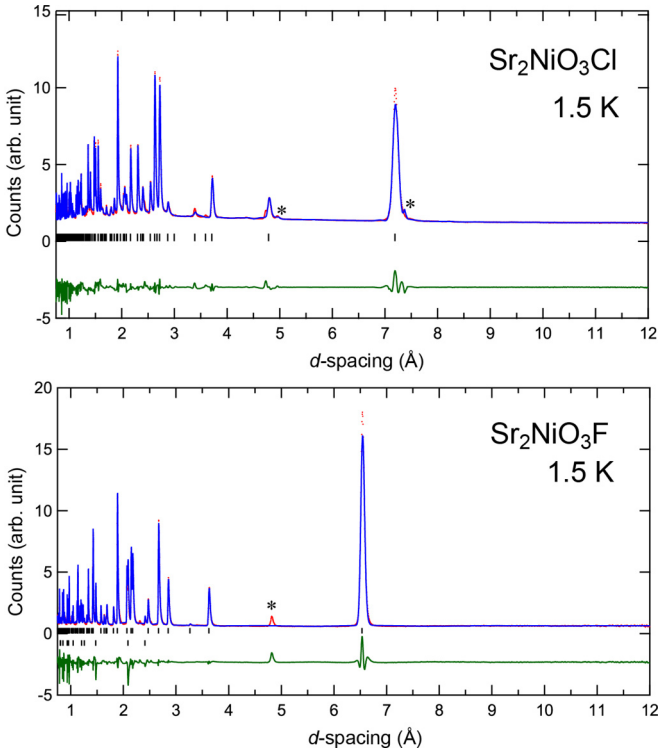

FIG. 2. Rietveld refinements against the neutron powder diffraction data of Sr_2NiO_3Cl and Sr_2NiO_3F collected at 1.5 K. Observed (dots), calculated (upper solid line), and difference (bottom solid line) plots are drawn. The asterisk represents uncharacterized peaks, which appeared even above 150 K ($\ll$ their phase transition temperatures).

B. Magnetic susceptibility and heat capacity

Figure 3 shows the temperature dependence of the magnetic susceptibility ($\chi = M/T$) of Sr_2NiO_3Cl and Sr_2NiO_3F measured at $H = 1$ kOe. These results are consistent with those previously reported [19]. The $\chi(T)$ of both oxyhalides increases with decreasing temperature and obey the Curie-Weiss law, $\chi(T) = C/(T-\theta)$, between 200 and 350 K, where C and θ denote the Curie constant and Weiss temperature, respectively. The C values of Sr_2NiO_3Cl and Sr_2NiO_3F are 0.4014(8) and 0.4861(5) emu K/mol, respectively. These values are consistent with those expected for 1 mol of $S = 1/2$ Ni^{3+} ions and $g = 2.1$, as determined by paramagnetic ESR

TABLE II. Crystallographic data for Sr_2NiO_3Cl and Sr_2NiO_3F obtained from Rietveld Refinement against neutron powder diffraction data at 5 K.

Sr_2NiO_3Cl: $P4/nmm$ (#129), a= 3.83918(5) Å, c= 14.3636(4) Å), R_{wp} = 10.8%, R_{Bragg} = 6.61%.

Atom	Site	Occupancy	x	y	z	B_{iso}/Å^2
Sr1	2*c*	1	0.75	0.75	0.0964(2)	0.22(9)
Sr2	2*c*	1	0.75	0.75	0.3407(3)	0.33(8)
Ni	2*c*	1	0.25	0.25	0.20805(1)	0.51(5)
O_{eq}	4*f*	1	0.25	0.75	0.22844(1)	0.37(6)
O_{ap}	2*c*	1	0.25	0.25	0.0754(3)	0.43(9)
Cl	2*c*	1	0.25	0.25	0.4237(2)	0.72(6)

Sr_2NiO_3F: $I4/mmm$ (#139), a = 3.77084(1) Å, c = 13.0616(4) Å), R_{wp} = 9.01%, R_{Bragg} = 5.24%.

Atom	Site	Occupancy	x	y	z	B_{iso}/Å^2
Sr	4*e*	1	0	0	0.3622(2)	0.86(9)
Ni	4*e*	0.5	0	0.5	0.0179(5)	0.75(10)
O_{eq}	4*c*	0.97(1)	0	0.5	0	1.21(12)
O_{ap}/F	4*e*	0.5/0.5	0	0	0.1721(3)	1.36(8)[a]

[a]B_{iso} values for O_{ap} and F were constrained to the same value.

measurements (see the Supplemental Material [42] for more details). The Weiss temperatures for Sr_2NiO_3Cl and Sr_2NiO_3F were 39.4(4) and 37.6(2) K, respectively. Both values indicate the presence of predominantly ferromagnetic interactions but are substantially larger than those previously reported [19]. The reason has not been made clear yet. However, from a comparison of the magnetic susceptibility and isothermal magnetization curves (see the Supplemental Material [42] for plots of isothermal magnetization curves), we found the magnetization of both oxyhalides is more enhanced than that in the previous report. Furthermore, a concave magnetization curve observed for Sr_2NiO_3Cl is typical of low-dimensional quantum antiferromagnets [43–45]. This behavior was not observed in the early study. These results suggest that the present sample quality has been improved, and thus the Weiss temperatures should be more precise. On further cooling from 200 K, the magnetic susceptibility of Sr_2NiO_3Cl exhibited a broad maximum centered at T_{max}= 35 K, indicating a short-range magnetic order; however, no indication of long-range magnetic ordering was discernible down to 2 K. In contrast, Sr_2NiO_3F exhibits spin-glass-like behavior with ZFC and FC data diverging below 12 K.

Figure 4 shows the total heat capacity (C_p) of both oxyhalides plotted as a function of temperature, measured under zero magnetic field. Despite the apparent differences in magnetic behavior between Sr_2NiO_3Cl and Sr_2NiO_3F, no clear difference or anomaly was observed in the C_p curves for either material down to 2 K. In the C_p/T vs T plot of Sr_2NiO_3Cl, a closer inspection revealed a broad hump between 20 and 50 K, as depicted in the inset of Fig. 4. This anomaly corresponds not only to the broad maximum observed in the magnetic susceptibility but also a static magnetic order at T_N= 28 K, which was unambiguously detected by μ^+SR measurements, as will be discussed in greater detail below.

C. High-field ESR

The temperature dependence of the ESR spectra of Sr_2NiO_3Cl at 160 GHz is plotted in Fig. 5(a), which clearly shows that the absorption line broadens as the temperature decreases, whereas the resonance field remains almost unchanged. The temperature dependence of the linewidths deduced from the spectra is shown in Fig. 5(b). The standard ESR theory relates the linewidth of ESR signals to the spin correlation function. Therefore, a rapid increase in the linewidth as the temperature falls below 40 K strongly suggests the formation of short-range magnetic order. As determined by μ^+SR measurements, the linewidth increases, even across T_N, at low temperatures. The absence of a linewidth divergence or an antiferromagnetic (AFM) resonance is probably due to suppression of long-range magnetic ordering or the use of a powder sample, which averages anisotropic g factors [46].

D. μ^+SR

To understand the local magnetic environments in Sr_2NiO_3Cl and Sr_2NiO_3F, μ^+SR experiments were performed on both samples. Figure 6 shows the ZF-μ^+SR spectra recorded at 2 K, the lowest temperature measured. Because the ZF-μ^+SR spectrum of Sr_2NiO_3Cl oscillates with multiple frequency components, a static, most likely long-range, magnetic order is unambiguously formed in Sr_2NiO_3Cl. On the other hand, the ZF-spectrum of Sr_2NiO_3F exhibits fast relaxation with only a first minimum at t = 0.03 μs. Such a spectrum suggests either the presence of a highly damped oscillation or a Kubo-Toyabe relaxation [47]: the highly damped oscillation implies the formation of a short-range static magnetic order, whereas the Kubo-Toyabe relaxation indicates the presence of randomly oriented localized magnetic moments. The μ^+SR results are explained in more detail below.

1. μ^+SR *on* Sr_2NiO_3Cl

Before analyzing the ZF-μ^+SR spectrum, the results of the weak TF (wTF)- μ^+SR measurements will be described to understand the overall nature of the antiferromagnetic transition. Here, "weak" indicates that the applied TF is smaller

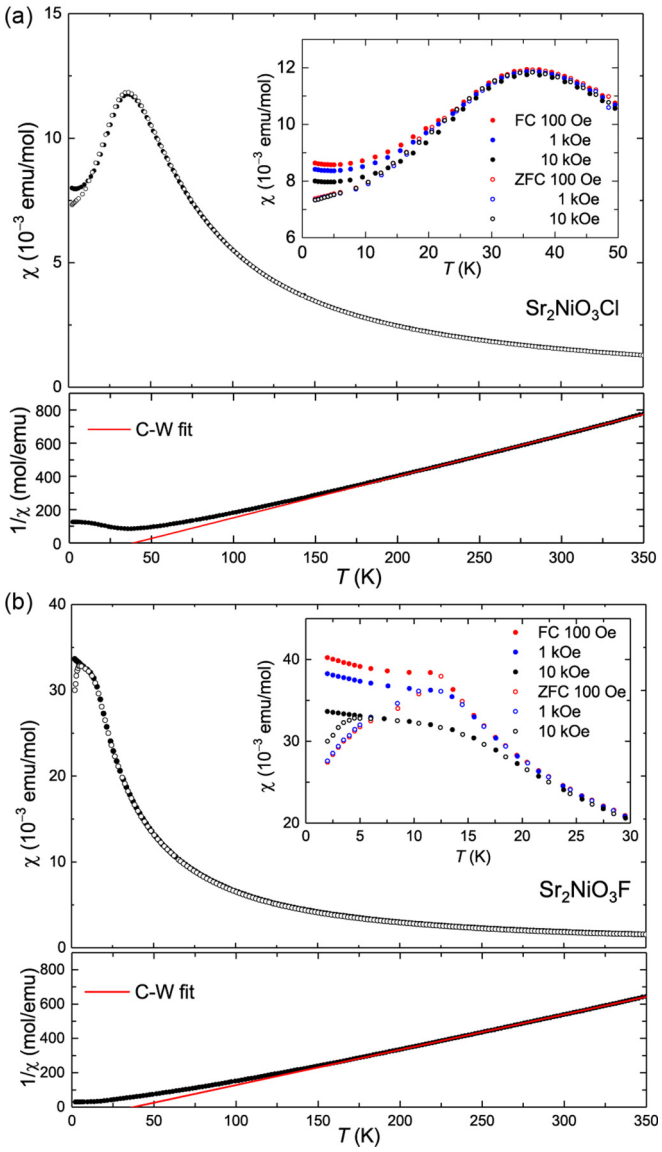

FIG. 3. Temperature dependence of the magnetic susceptibility and its inverse for (a) Sr_2NiO_3Cl and (b) Sr_2NiO_3F, measured under zero-field and field-cooled conditions. The solid lines represent Curie-Weiss fitting lines. In the insets, the data in a low temperature region are highlighted.

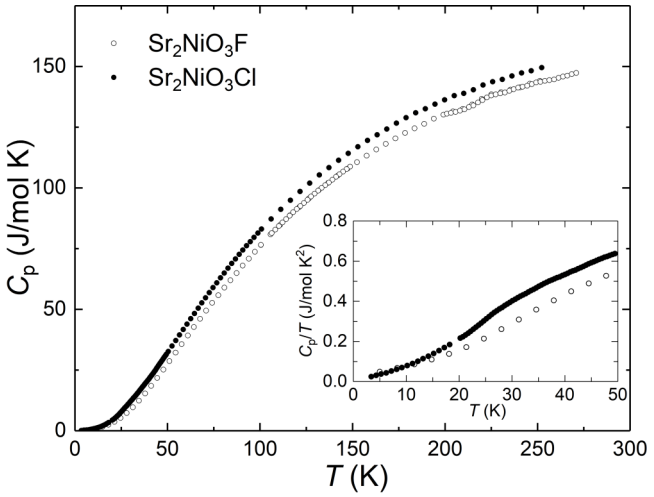

FIG. 4. Heat capacity of Sr_2NiO_3Cl and Sr_2NiO_3F measured under zero magnetic field. The inset shows the C_p/T vs T plots.

than the internal magnetic fields at the muon sites generated by the magnetically ordered state.

Figure 7 shows the temperature variation in the wTF-μ^+SR spectrum recorded at wTF= 50 Oe. At 60 K, the wTF-μ^+SR spectrum exhibited an oscillation with a full amplitude, or asymmetry of 0.23, indicating that the entire sample was in a paramagnetic state. As the temperature decreases from 60 K, the asymmetry decreases owing to the emergence of an internal AF magnetic field with a magnitude far exceeding that of the wTF. To precisely capture the temperature variation in the wTF-μ^+SR spectrum, the spectrum was fitted with a combination of an exponentially relaxing cosine oscillation and an exponentially relaxing nonoscillatory signal:

$$A_0 P_{TF}(t) = A_{\rm TF} e^{-\lambda_{\rm TF} t} \cos(\omega_{\rm TF} t + \varphi_{\rm TF}) + A_{\rm M} e^{-\lambda_{\rm M} t}, \quad (1)$$

where A_0 is the initial ($t = 0$) asymmetry, $P_{\rm TF}(t)$ is the muon spin polarization function in the wTF, $A_{\rm TF}$ and $A_{\rm M}$ are the asymmetries of the two signals, $\omega_{\rm TF}$ is the muon spin precession frequency owing to the applied wTF, $\phi_{\rm TF}$ is the initial phase of the oscillation signal, $\lambda_{\rm TF}$ and $\lambda_{\rm M}$ are the exponential relaxation rates. The wTF oscillation signal is caused by muons stopped in paramagnetic phases, and thus the normalized asymmetry ($= A_{\rm TF}/A_0$) is roughly proportional to the paramagnetic volume fraction in a sample.

Figures 8(a) and 8(b) show the temperature dependences of $A_{\rm TF}$, $A_{\rm M}$, $\lambda_{\rm TF}$, and $\lambda_{\rm M}$. As the temperature decreases from 60 K, the $A_{\rm TF}$ is nearly independent of temperature down to approximately 30 K, then begins to decrease rapidly down to 20 K, and then roughly stabilizes to a constant value (approximately 0.05) down to 2 K. This indicates the occurrence of a sharp magnetic transition at approximately 27 K, whereas a non-zero $A_{\rm TF}$, even at 2 K, suggests the presence of paramagnetic phases, or impurity phases, in the sample. The fit of the $A_{\rm TF}(T)$ curve with a sigmoid function indicated that $T_{\rm N} = 27.7(1.2)$ K for Sr_2NiO_3Cl. This value agrees with the C_p results. In contrast, $A_{\rm M}$ is zero between 30 and 60 K, then increases rapidly with decreasing temperature from 30 K. However, $A_{\rm M}$ decreases as temperature decreases further and approaches temperature independence below 25 K. Because $A_{\rm M}$ at 2 K (~ 0.07) is close to 1/3 of the $A_{\rm TF}$ of the S_2NiO_3Cl phase (~ 0.19), $A_{\rm M}$ corresponds to the tail signal from the powder sample in the magnetically ordered phase. That is, for a powder sample without orientation, the internal magnetic field in a magnetically ordered phase is parallel to the initial muon spin polarization for 1/3 of powder particles, leading to a nonoscillatory relaxing signal, i.e., a 1/3 tail signal, while the other 2/3 provide an oscillatory signal. In other words, $A_{\rm M}$ corresponds to the longitudinal component, where the internal AF field is parallel to the initial muon polarization. On the other hand, $A_{\rm M}$ includes both longitudinal and transverse components above $T_{\rm N}$ owing to the large fluctuations in the AF field at the transition.

As shown in Fig. 8(b), the $\lambda_{\rm TF}(T)$ curve exhibits a small maximum below the vicinity of $T_{\rm N}$. Below 20 K, $\lambda_{\rm TF}$ is

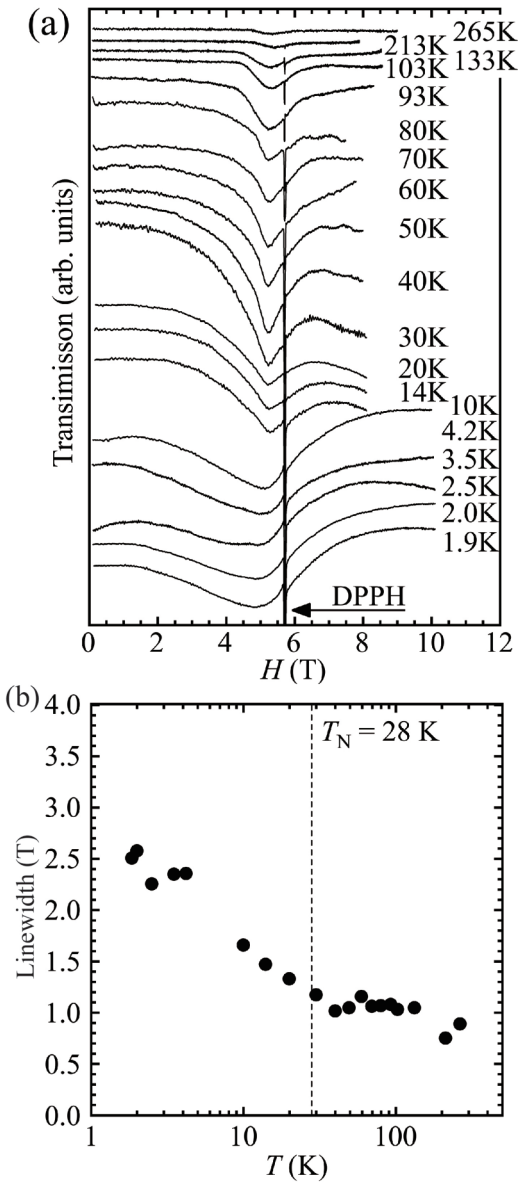

FIG. 5. Temperature dependence of (a) ESR spectra and (b) linewidth at 160 GHz observed for Sr_2NiO_3Cl. Sharp absorption lines are DPPH signals as field marker for $g = 2$.

roughly temperature-independent, implying that the impurity phases are not magnetic. Although λ_M exhibits a clear maximum at T_N owing to a critical phenomenon of the AF transition, λ_M decreases with decreasing temperature below T_N. This is consistent with the tail signal, for which the relaxation rate approaches zero at low temperatures because thermal fluctuations are suppressed.

The ZF-μ^+SR spectrum for Sr_2NiO_3Cl (Fig. 6) was fitted with the sum of three Gaussian relaxing cosine oscillations and an exponentially relaxing nonoscillatory signal:

$$A_0 P_{ZF}(t) = \sum_{n=1}^{3} A_{AF,n} e^{-\sigma_{AF,n}^2 t^2} \cos(\omega_{AF,n} t + \varphi_{AF,n}) + A_{tail} e^{-\lambda_{tail} t}, \quad (2)$$

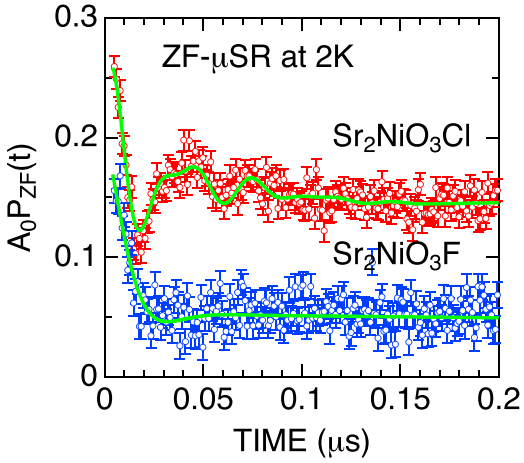

FIG. 6. The ZF-μ^+SR spectra for Sr_2NiO_3Cl and Sr_2NiO_3F recorded at 2 K. (2) for Sr_2NiO_3Cl and Eq. (3) for Sr_2NiO_3F. The spectrum for Sr_2NiO_3Cl is shifted upward by 0.1 for clarity of display.

where $P_{ZF}(t)$ is the muon spin polarization function in ZF, $A_{AF,n}(n = 1–3)$ and A_{tail} are the asymmetries of the precession signals and longitudinal component of the AF phase, $\sigma_{AF,n}$, $\omega_{AF,n}$, $\phi_{AF,n}$, and λ_{tail} are the Gaussian relaxation rate, muon Larmor frequencies corresponding to the AF internal magnetic fields, initial phases of the muon precessing signals, and exponential relaxation rate, respectively. As depicted in Fig. 8(c), as the temperature increased from 2 K, the three muon precession frequencies $f_{AF,n}(= \omega_{AF,n}/2\pi)$ decreased gradually and disappeared at approximately 22 K, which is below the vicinity of T_N. The three $f_{AF,n}$ values indicated the presence of three magnetically distinct muon sites in the Sr_2NiO_3Cl lattice, although the three sites could be one crystallographic site [48]. The fact that the temperature at which all three $f_{AF,n}$ disappear is approximately 5 K lower than T_N determined with wTF-μ^+SR, suggests the presence of an intermediate phase, such as an incommensurate AF phase between 22 K and T_N [49].

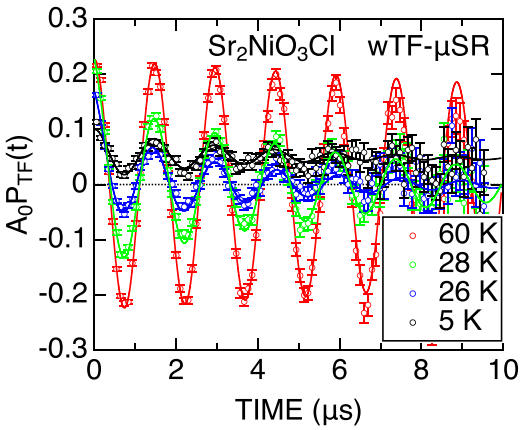

FIG. 7. The temperature variation in the wTF-μ^+SR spectra for Sr_2NiO_3Cl recorded at 60, 28, 26, and 5 K with applied TF of 50 Oe. Solid lines represent the best fit using Eq. (1). The offset of the spectrum at 5 K corresponds to the 1/3 tail component of the powder sample in the magnetic ordered state.

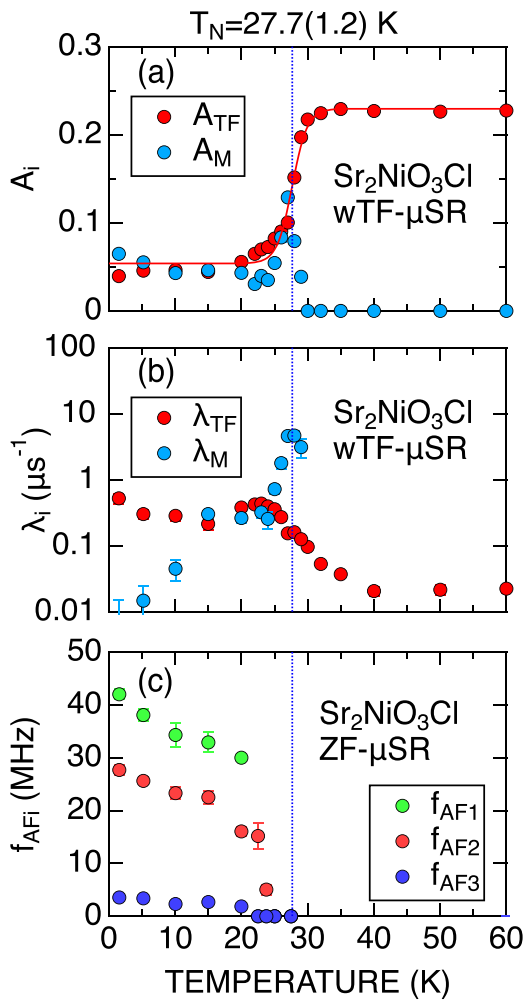

FIG. 8. The temperature dependence of the wTF- and ZF-μ^+SR parameters for Sr_2NiO_3Cl: (a) the two asymmetries, A_{TF} and A_M, (b) their exponential relaxation rate λ_{TF} and λ_M, and (c) the three muon precession frequencies in the AF ordered phase. Vertical blue dotted lines represent T_N determined by the Sigmoid fit of the $A_{TF}(T)$ curve, which is also shown in (a) as a red solid line.

2. μ^+SR *on* Sr_2NiO_3F

In contrast to Sr_2NiO_3Cl, the ZF-μ^+SR spectrum for Sr_2NiO_3F at 2 K exhibits a rapid damping with a first minimum at $t \sim 0.03$ μs (see Fig. 6), indicating the presence of an internal magnetic field with a wide field distribution. In order to determine whether the magnetic moments are randomly oriented or ordered, the LF-μ^+SR spectra were recorded at LF = 1000 and 2000 Oe, while the LF spectrum is usually used to check whether the internal magnetic field is static or dynamic. A Kubo-Toyabe fitting function is applicable for a random magnetic field, whereas the damped cosine function is suitable for an ordered state. Figure 9 shows the ZF- and LF-μ^+SR spectra together with the best fits using a static Gaussian Kubo-Toyabe function [$G_{ZZ}^{KT}(t, \Delta, H_{LF})$], which describes the time evolution of the muon spin polarization owing to the internal magnetic field formed by randomly oriented static dipoles with a Gaussian distribution [33], where Δ denotes the field distribution width. Although the two LF-μ^+SR spectra

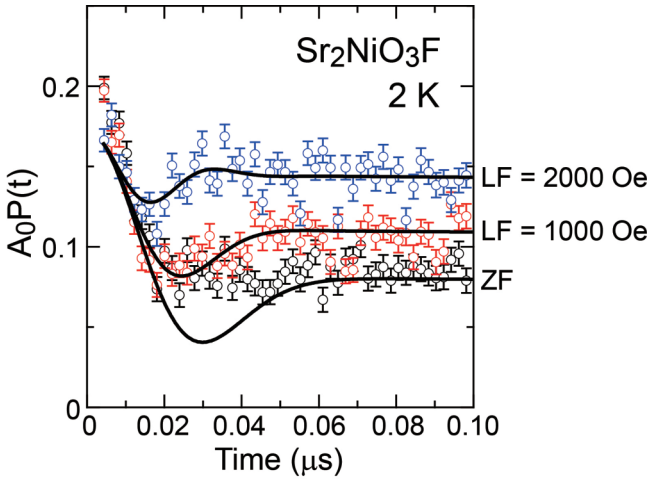

FIG. 9. (a) The ZF and LF-μ^+SR spectra for Sr_2NiO_3F recorded at 2 K. Solid lines represent the best fit using a Kubo-Toyabe function.

were reasonably fitted with $G_{ZZ}^{KT}(t, \Delta, H_{LF})$, the ZF-$\mu^+$SR spectrum was not. This implies that the internal magnetic field observed in ZF is not caused by random moments but rather caused by AF short-range magnetic order. However, this AF internal magnetic field is so weak that application of LF is sufficient to decouple the effect of the AF internal magnetic field [50]. Therefore, the ZF-μ^+SR spectrum was fitted with an exponentially relaxing cosine oscillation, as in the case of Sr_2VO_4 [51]:

$$A_0 P_{ZF}(t) = A_{AF} e^{-\lambda_{AF} t} \cos(\omega_{AF} t + \varphi_0) + A_{tail} e^{-\lambda_{tail} t}, \quad (3)$$

where A_{AF} and A_{tail} are the asymmetries of the two signals and λ_{AF} and λ_{tail} are their exponential relaxation rates. $f_{AF}(= \omega_{AF}/2\pi)$ is the muon Larmor frequency corresponding to the AF internal field, and ϕ_0 is the initial phase. It should be emphasized that this fit assumes the formation of an AF short-range order in Sr_2NiO_3F.

Figure 10 shows the temperature dependence of the wTF- and ZF-μ^+SR parameters of Sr_2NiO_3F. The wTF-μ^+SR spectrum was fitted using Eq. (1). The $A_{TF}(T)$ curve demonstrated that Sr_2NiO_3F entered a magnetically ordered phase below approximately 18 K. The sigmoid fit of the $A_{TF}(T)$ curve indicated that $T_N = 18.1$ (1.3) K. As the temperature decreases from 30 K, the $A_M(T)$ curve also indicates an increase in the volume of the AF ordered phase toward T_N, and then A_M levels off to a constant value at approximately 2/3 of the A_{TF}(30 K). Considering the magnitude of λ_M, the A_M corresponds to the asymmetry of the transverse component of the ordered AF phase, i.e., $A_M = A_M^{trans}$. The $\lambda_{TF}(T)$ curve shows a clear maximum below the vicinity of T_N, whereas λ_M increases with decreasing temperature, even below T_N. However, the λ_{AF} determined from the ZF-μ^+SR measurement suggests that the fluctuation of the internal AF field levels off to approximately 50 μs^{-1} below approximately 14 K. This also suggests that λ_{AF} of the longitudinal component (λ_{tail}) is very small, providing a temperature-independent background signal for A_{tail}. Below 14 K, f_{AF} appears and gradually increases with decreasing temperature, which is consistent with the order parameter of the AF transition.

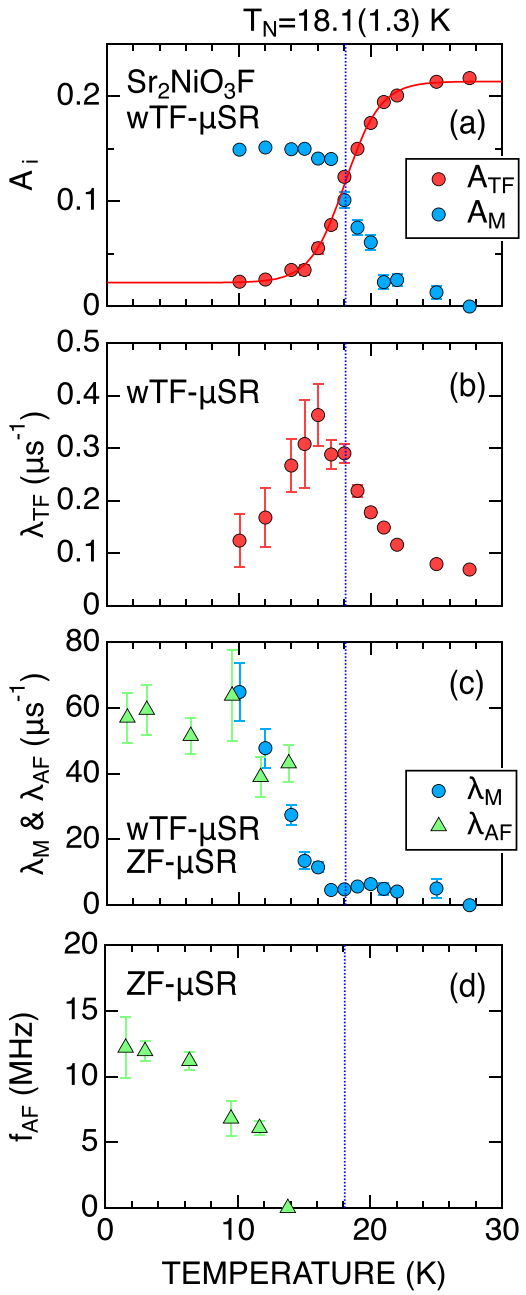

FIG. 10. The temperature dependence of the wTF- and ZF-μ^+SR parameters for Sr_2NiO_3F: (a) the two asymmetries, A_{TF} and A_M, (b) the exponential relaxation rate of the ATF signal (λ_{TF}), (c) the exponential relaxation signal of the AM signal (λ_M) and the AF oscillatory signal (λ_{AF}), and (4) the muon precession frequency in the AF ordered phase (f_{AF}). Vertical blue dotted lines represent T_N determined by the Sigmoid fit of the $A_{TF}(T)$ curve, which is also shown in (a) as a red solid line.

E. First-principles calculations

The μ^+SR measurements clearly demonstrated a static magnetic ordering in Sr_2NiO_3Cl; however, information on the magnetic structure is still limited. To gain a deeper understanding of the relationship between the dominant ferromagnetic (FM) interactions and magnetic structure, we performed DFT + U calculations on four magnetically ordered models: FM, AFM-1 (ferromagnetic layers stacked antiferromagnetically), AFM-2 [ferromagnetic chains arranged antiferromagnetically in the two-dimensional magnetic plane], and AFM-3 states (the nearest neighbor spins aligned antiferromagnetically) (see Fig. 11). As shown in Table III, our calculations show that the FM state is the most stable of all the spin models that we assumed. Given the lack of a ferromagnetic signal in the magnetic susceptibility of $SrNiO_3Cl$ and the limitation of DFT calculations for strongly correlated electron systems, the AFM-1 (the second most stable magnetic state) is a more plausible model. In fact, the ferromagnetic spin arrangement in the NiO_2 plane in the model is consistent with the dominant FM interactions

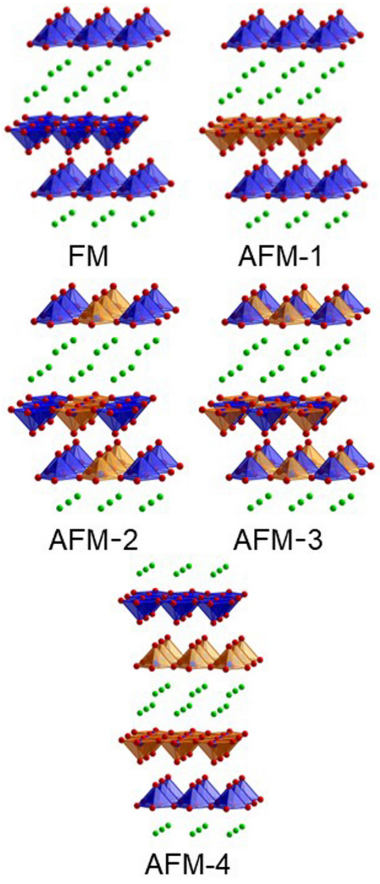

FIG. 11. Schematic representations of the FM, AFM-1, AFM-2, AFM-3, and AFM-4 type spin arrangements of Sr_2NiO_3Cl. Sr atom is omitted for clarity. In the AFM-1 model, each ferromagnetic layer is antiferromagnetically coupled along the c axis. The AFM-2 model forms a strip ordered arrangement in the NiO_2 plane. In the AFM-3 model, the nearest neighbor spins are aligned antiferromagnetically. The AFM-4 model is similar to the AFM-1 one except that the interlayer exchange interactions across the SrCl layers are ferromagnetically coupled.

TABLE III. Total energy difference per Ni (ΔE) of the three different ordered spin states of Sr_2NiO_3Cl determined from the DFT + U calculations ($U = 4$ eV). The values are given in meV relative to the energy of the FM state.

AFM-1	AFM-2	AFM-3
22	69	140

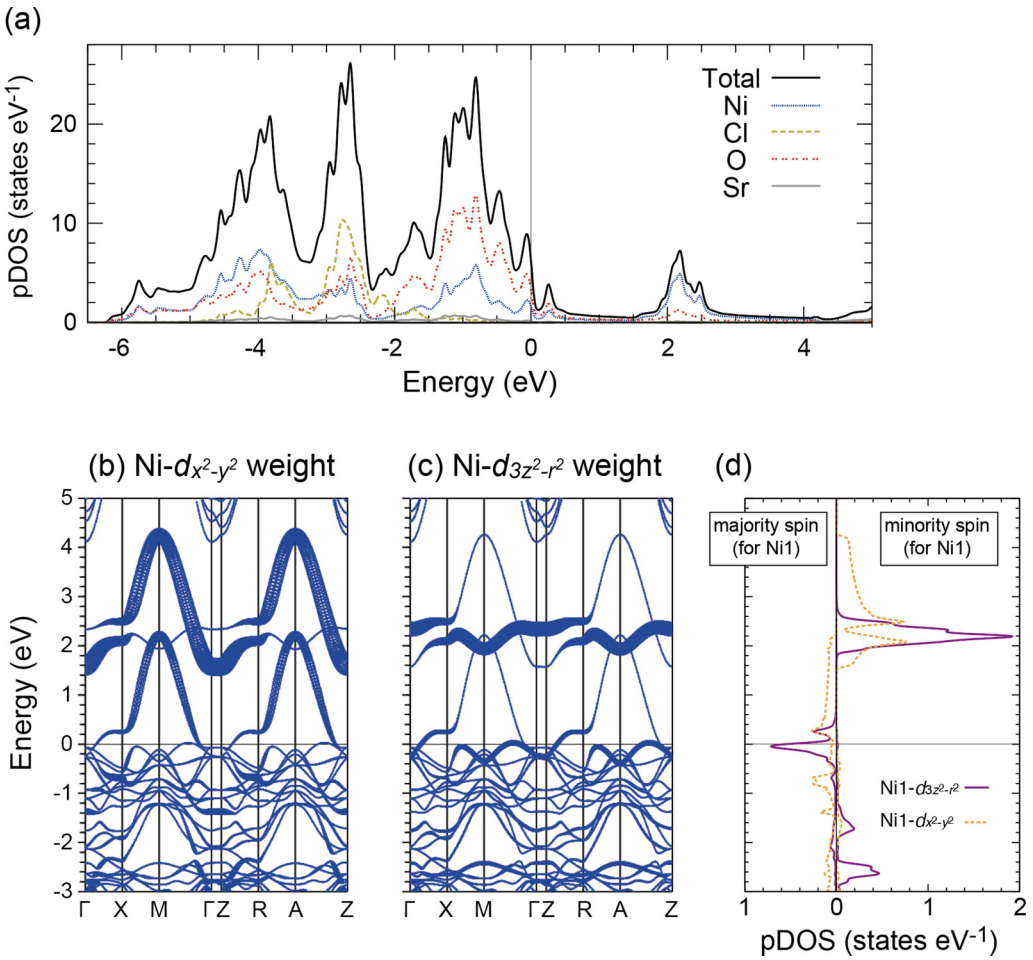

FIG. 12. (a)(d) Total DOS and partial DOS (pDOS) and (b)(c) band structures of Sr_2NiO_3Cl with AFM-1 spin arrangement. The atom-decomposed pDOS is shown in (a), and the spin-decomposed pDOS is shown in (d), where the dx^2-y^2 and $d3z^2$-r^2 orbitals at a certain Ni site denoted as Ni1 is focused. (b) The dx^2-y^2 and (c) $d3z^2$-r^2-weighted bands are highlighted with bold solid lines.

suggested by the magnetic susceptibility measurements. For the AFM-1 state, the magnitude of the spin polarization on the Ni site was calculated as 1.15 μ_B, which also agrees with the low-spin state of Ni^{3+}. Figure 12(a) shows the total and partial DOS of Sr_2NiO_3Cl, which reveal a strong hybridization between O $2p$ and Ni $3d$ states in the valence bands in contrast to a weak hybridization between Cl $3p$ and Ni $3d$ states. Based on the calculated band structures shown in Figs. 12(b)–12(c) and the spin-decomposed partial DOS of Ni $d_{3z^2-r^2}$ and $d_{x^2-y^2}$ orbitals shown in Fig. 12(d), we can see that the $d_{3z^2-r^2}$ bands are almost half-filled. For the $d_{x^2-y^2}$ bands, the majority spin bands are less occupied than those of $d_{3z^2-r^2}$ orbitals. Therefore, the antiferromagnetic and insulating properties of $SrNiO_3Cl$ can be interpreted well by the AFM-1 spin model. We note that the half-filled occupation of the $d_{3z^2-r^2}$ bands disagrees with a previous model in which the d_{xy} orbital is half-occupied [19].

IV. DISCUSSION

In this section, we will discuss the origin of the involved magnetic interactions, especially the dominant FM interactions and the difference in magnetic ground states. The half-filled $d_{3z^2-r^2}$ orbital of Ni^{3+} suggested by theoretical calculations differs from that proposed by a previous study. Notably, this orbital order also differs from that observed in the ferromagnetic copper fluoride K_2CuF_4 [25]. In the present spin configuration, the J_2 interaction on a NiO_4 square could be even smaller than the J_1 interaction because the $d_{3z^2-r^2}$ orbital is directed along the c-axis direction. Therefore, J_1 interaction can be expected to be the main source of FM interaction. The values of the J_1 and J_2 spin exchange parameters in the Heisenberg mode, $H = \sum_{i,j} J_{ij} \boldsymbol{S_i} \cdot \boldsymbol{S_j}$, were calculated from AFM-1, -2, -3 models, yielding −34 meV (FM) and 4 meV (AFM), respectively . The FM J_1 is dominant over the AFM J_2, as we expected. The FM interaction can be rationalized by considering the interaction between half-occupied $d_{3z^2-r^2}$ and unoccupied $d_{x^2-y^2}$ orbitals. The strong σ bonding between the O $2px$ and Ni $d_{x^2-y^2}$ orbitals and the Hund coupling on the Ni atom would energetically favor charge transfer from the $d_{3z^2-r^2}$ to $d_{x^2-y^2}$ orbitals, resulting in the parallel alignment of the nickel spins. (Fig. 13). On the other hand, the interlayer AFM interaction can be explained by considering the superexchange interactions between $d_{3z^2-r^2}$ orbitals across the SrO or SrCl rocksalt layers. Note that a magnetic structure model with ferromagnetic interlayer interactions across the SrCl rocksalt layers (AFM-4)

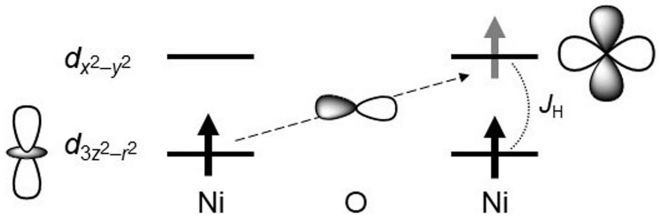

FIG. 13. Schematic of the superexchange pathway driving a ferromagnetic interaction between the nickel spins. J_H stands for Hund coupling, which aligns spin moments in two different orbitals parallel.

cannot be ruled out. In fact, the total energy of the AFM-4 model was found to be comparable to that of AFM-1; the difference between them is less than 1 meV, indicating that the interlayer interaction through SrCl layers is negligible in comparison to that through SrO layers. This can also be expected from the bond distances between the Ni atoms (6.5644 Å across the SrO layers and 8.815 Å across the SrCl layers). In Sr_2FeO_3F isostructural with Sr_2NiO_3Cl, the inequivalence of interlayer exchange interactions leads to a complex orthogonal spin arrangement where La_2CuO_4-type stacking across the SrO layers competes with La_2NiO_4-type stacking across the SrF layers [52]. The inequivalent muon sites and possible existence of an intermediate phase in Sr_2NiO_3Cl may result from similar competition between interlayer exchange interactions through different anions.

At present, the origin of short-range order in Sr_2NiO_3F is not clear. However, based on the preceding discussion, the coexistence of FM and AFM intralayer interactions is essential. As depicted in Fig. 1, 1O/F site disordering produces the mixed-anion rocksalt layer SrOF, resulting in inhomogeneous interlayer exchange interactions. In addition, the substitution of fluorine for chlorine reduces the Ni-Ni interlayer distances (6.616–7.497 Å); thus, the influence of interlayer exchange interactions via fluoride ions on the magnetic properties cannot be ignored. If the interlayer exchange interactions across SrF or SrOF rocksalt *fragments* are ferromagnetically coupled, the FM and AFM domains within the NiO_2 plane would compete with one another.

V. CONCLUSION

We investigated the magnetic properties of quantum spin square-lattice antiferromagnets, Sr_2NiO_3Cl and Sr_2NiO_3F, with ordered and disordered halogen sites at the apical sites, respectively. μ^+SR measurements revealed a static, mostly long-range, magnetic order below 28 K for Sr_2NiO_3Cl and a short-range magnetic order below 18 K for Sr_2NiO_3F. First-principles calculations for several spin state models showed that the $d_{3z^2-r^2}$ orbital was half-filled and the AFM-1 type spin arrangement (ferromagnetic NiO_2 layers stacked antiferromagnetically) could explain the dominant FM interactions in the oxyhalides, as suggested by the magnetic susceptibility measurements. To describe the reason for the destruction of long-range magnetic order in the oxyfluoride, the competition between the AFM interlayer interactions via O^{2-} ions and the FM interactions via F^- ions should be considered. Magnetic structure determination via neutron scattering is important for characterizing the relationship between the exchange interactions between nickel spins and the relevant magnetic ground states. We would like to emphasize that the magnetism of the present oxyhalides is distinct from those of $S = 1/2$ square-lattice copper-based compounds such as La_2CuO_4 and Sr_2CuO_2Cl with the $d_{x^2-y^2}$ orbital being half-occupied. The stabilization of $d_{3z^2-r^2}$ orbital order by multiple anions could provide a new venue for studying novel quantum spin phenomena that could not be induced by other d orbitals.

The authors declare no competing financial interest.

ACKNOWLEDGMENTS

This study was partially supported by the Japan Society for the Promotion of Science KAKENHI (Grants No. JP20H05276, No. JP22H04601, No. JP18H01863, and No. JP20K21149) and Core-to-Core Program (JPJSCCA20200004). Y.T. acknowledges the grant from the Murata Science Foundation. A.T.B. was supported by the Engineering and Physical Sciences Research Council (Grant No. EP/T027991/1). We thank the staff of PSI for their help with the μ^+SR experiments (Proposal No. 20131798). Neutron diffraction experiments were performed at the WISH beamline at ISIS (Proposal No. RB1710046).

[1] C. Broholm, R. J. Cava, S. A. Kivelson, D. G. Nocera, M. R. Norman, and T. Senthil, Quantum spin liquids, Science **367**, eaay0668 (2020).

[2] A. Vasiliev, O. Volkova, E. Zvereva, and M. Markina, Milestones of low-D quantum magnetism, npj Quantum Mater. **3**, 18 (2018).

[3] E. Manousakis, The spin-½ Heisenberg antiferromagnet on a square lattice and its application to the cuprous oxides, Rev. Mod. Phys. **63**, 1 (1991).

[4] N. Tsyrulin, T. Pardini, R. R. Singh, F. Xiao, P. Link, A. Schneidewind, A. Hiess, C. P. Landee, M. M. Turnbull, and M. Kenzelmann, Quantum effects in a weakly frustrated $S = 1/2$ two-dimensional Heisenberg antiferromagnet in an applied magnetic field, Phys. Rev. Lett. **102**, 197201 (2009).

[5] A. de la Torre *et al.*, Mirror symmetry breaking in a model insulating cuprate, Nat. Phys. **17**, 777 (2021).

[6] T. Hanaguri, C. Lupien, Y. Kohsaka, D.-H. Lee, M. Azuma, M. Takano, H. Takagi, and J. C. Davis, A "Checkerboard" electronic crystal state in lightly hole-doped $Ca_{2-x}Na_xCuO_2Cl_2$, Nature (London) **430**, 1001 (2004).

[7] P. W. Anderson, The resonating valence bond state in La_2CuO_4 and superconductivity, Science **235**, 1196 (1986).

[8] N. Shannon, T. Momoi, and P. Sindzingre, Nematic Order in Square Lattice Frustrated Ferromagnets, Phys. Rev. Lett. **96**, 027213 (2006).

[9] N. Shannon, B. Schmidt, K. Penc, and P. Thalmeier, Finite temperature properties and frustrated ferromagnetism in a square lattice Heisenberg model, Eur. Phys. J. B **38**, 599 (2004).

[10] P. Chandra and B. Doucot, Possible spin-liquid state at large s for the frustrated square Heisenberg lattice, Phys. Rev. B **38**, 9335(R) (1988).

[11] L. Siurakshina, D. Ihle, and R. Hayn, Magnetic order and finite-temperature properties of the two-dimensional frustrated Heisenberg model, Phys. Rev. B **64**, 104406 (2001).

[12] S. Morita, R. Kaneko, and M. Imada, Quantum spin liquid in spin 1/2 $J_1 - J_2$ Heisenberg model on square Lattice: many-variable variational monte carlo study combined with quantum-number projections, j. Phys. Soc. Jpn. **84**, 11 (2015).

[13] A. A. Tsirlin, A. A. Belik, R. V. Shpanchenko, E. V. Antipov, E. Takayama-muromachi, and H. Rosner, Frustrated spin-1/2 square lattice in the layered perovskite $PbVO_3$, Phys. Rev. B **77**, 092402 (2008).

[14] K. Oka, I. Yamada, M. Azuma, S. Takeshita, K. H. Satoh, A. Koda, R. Kadono, M. Takano, Y. Shimakawa, and M. Curie, Magnetic Ground-State of Perovskite PbVO 3 with Large Tetragonal Distortion, Inorganic Chemistry **47**, 7355 (2008).

[15] O. Mustonen, S. Vasala, E. Sadrollahi, K. P. Schmidt, C. Baines, H. C. Walker, I. Terasaki, F. J. Litterst, E. Baggio-Saitovitch, and M. Karppinen, Spin-Liquid-like state in a Spin-1/2 square-lattice antiferromagnet perovskite induced by d^{10}–d^0 cation mixing, Nat. Commun. **9**, 1085 (2018).

[16] O. Mustonen, S. Vasala, K. P. Schmidt, E. Sadrollahi, H. C. Walker, I. Terasaki, F. J. Litterst, E. Baggio-Saitovitch, and M. Karppinen, Tuning the $S = 1/2$ square lattice antiferromagnet $Sr_2Cu(Te_{1-x}W_x)O_6$ from Néel order to quantum disorder to columnar order, Phys. Rev. B **98**, 064411 (2018).

[17] M. Watanabe, N. Kurita, H. Tanaka, W. Ueno, K. Matsui, and T. Goto, Valence-Bond-Glass state with a singlet gap in the Spin-1/2 square-lattice random $J_1 - J_2$ Heisenberg antiferromagnet $Sr_2Cu\,Te_{1-x}W_xO_6$, Phys. Rev. B **98**, 054422 (2018).

[18] K. Uematsu and H. Kawamura, Randomness-induced quantum spin liquid behavior in the $s = \frac{1}{2}$ random $J_1 - J_2$ Heisenberg antiferromagnet on the square lattice, Phys. Rev. B **98**, 134427 (2018).

[19] Y. Tsujimoto, K. Yamaura, and T. Uchikoshi, Extended Ni(III) oxyhalide perovskite Derivatives: Sr_2NiO_3X (X = F, Cl), Inorg. Chem. **52**, 10211 (2013).

[20] R. D. Shannon, Revised effective ionic radii and systematic studies of interatomic distances in halides and chalcogenides, Acta Crystallogr., Sect. A **32**, 751 (1976).

[21] S. E. McLain, M. R. Dolgos, D. A. Tennant, J. F. C. Turner, T. Barnes, T. Proffen, B. C. Sales, and R. I. Bewley, Magnetic behaviour of layered Ag fluorides, Nat. Mater. **5**, 561 (2006).

[22] I. Yamada, Magnetic properties of K_2CuF_4 –A transparent two-dimensional Ferromagnet–, J. Phys. Soc. Jpn. **33**, 979 (1972).

[23] C. Dekker, A. F. M. Arts, and H. W. de Wijn, Magnetic order in the two-dimensional randomly mixed ferromagnet-antiferromagnet $Rb_2Cu_{1-x}Co_xF_4$, Phys. Rev. B **38**, 11512 (1988).

[24] S. Sasaki, N. Narita, and I. Yamada, Preparation and magnetic susceptibility of Cs_2CuF_4 and Rb_2CuF_4, J. Phys. Soc. Jpn. **64**, 2701 (1995).

[25] D. I. Khomskii and K. I. Kugel, Orbital and magnetic structure of two-dimensional ferromagnets with Jahn-Teller ions, Solid State Commun. **13**, 763 (1973).

[26] Y. Ito and J. Akimitsu, Observation of orbital ordering in K_2CuF_4, J. Phys. Soc. Jpn. **40**, 1333 (1976).

[27] H. Manaka, T. Koide, T. Shidara, and I. Yamada, Observation of polarization-dependent x-ray absorption spectra arising from Cu $3d-$F$2p$ hybridization in the two-dimensional ferromagnets A_2CuF_4 (A = K, Cs), Phys. Rev. B **68**, 184412 (2003).

[28] C. Lee, J. Shim, and M. Whangbo, Cause for the orbital ordering of Cs_2AgF_4 and its effect on thermoelectric properties, Inorg. Chem. **57**, 11895 (2018).

[29] L. C. Chapon *et al.*, Wish: The new powder and single crystal magnetic diffractometer on the second target station, Neutron News **22**, 22 (2011).

[30] J. Rodríguez-Carvajal, Recent advances in magnetic structure determination by neutron powder diffraction, Physica B **192**, 55 (1993).

[31] M. Motokawa, H. Ohta, and N. Maki, Submillimeter EPR of Co:Rb_2MgF_4 and anomalous g-values, Int. J. Infrared Millim. Terahertz Waves **12**, 149 (1991).

[32] S. Kimura, H. Ohta, M. Motokawa, S. Mitsudo, W.-J. Jang, M. Hasegawa, and H. Takei, Submillimeter wave ESR measurements of metamagnetic Y_2Cu_2O, Int. J. Infrared Millim. Terahertz Waves **17**, 833 (1996).

[33] H. Nakagawa, N. Yamada, T. Akioka, K. Okubo, S. Kimura, and S. Ohta, Millimeter and submillimeter wave ESR System: Using 30 t pulsed magnetic field, Int. J. Infrared Millim. Terahertz Waves **19**, 167 (1998).

[34] P. D. Yaouanc and A. de Réotier, *Muon Spin Rotation, Relaxation, and Resonance, Application to Condensed Matter* (Oxford University Press, Oxford, 2011).

[35] G. M. Kalvius, D. R. Noakes, and O. Hartmann, *Chapter 206* μSR *Studies of Rare-Earth and Actinide Magnetic Materials, in Handbook on the Physics and Chemistry of Rare Earths* (North-Holland, Amsterdam, 2001), pp. 55–451.

[36] B. M. Suter and A. Wojek, Afree platform-independent framework for μSR data analysis, Phys. Proceedia **30**, 69 (2012).

[37] L. D. Marks, P. Blaha, K. Schwarz, G. K. H. Madsen, D. Kvasnicka, J. Luitz, R. Laskowski, and F. Tran, *WIEN2k, An Augmented Plane Wave + Local Orbitals Program for Calculating Crystal Properties*, in edited by K. Schwarz (Vienna University of Technology, Austria, 2018).

[38] P. Blaha, K. Schwarz, F. Tran, R. Laskowski, G. K. H. Madsen, and L. D. Marks, WIEN2k: An APW + LO program for calculating the properties of solids, J. Chem. Phys. **152**, 074101 (2020).

[39] J. P. Perdew, K. Burke, and M. Ernzerhof, Generalized Gradient Approximation Made Simple, Phys. Rev. Lett. **77**, 3865 (1996).

[40] V. I. Anisimov, I. v. Solovyev, M. A. Korotin, M. T. Czyżyk, and G. A. Sawatzky, Density-Functional theory and NiO photoemission spectra, Phys. Rev. B **48**, 16929 (1993).

[41] M. T. Czyżyk and G. A. Sawatzky, Local-Density functional and on-Site Correlations: The electronic structure of La_2CuO_4 and $LaCuO_3$, Phys. Rev. B **49**, 14211 (1994).

[42] See Supplemental Material at http://link.aps.org/supplemental/10.1103/PhysRevMaterials.6.114404 for additional neutron powder diffraction data, isothermal magnetization data, and electron paramagnetic resonance data. The Supplemental Material cites Ref. [19].

[43] H. Aruga katori, Y. Ajiro, T. Asano, and T. Goto, Nonlinear magnetization of a quasi-one-dimensional triangular-lattice antiferromagnet $CsNiCl_3$ up to 110 tesla, J. Phys. Soc. Jpn. **64**, 3038 (1995).

[44] Y. Hosokoshi, Y. Nakazawa, K. Inoue, K. Takizawa, H. Nakano, M. Takahashi, and T. Goto, Magnetic properties of low-dimensional quantum spin systems made of stable organic biradicals PNNNO, F_2 PNNNO, and PIMNO, Phys. Rev. B **60**, 12924 (1999).

[45] M. Hase, H. Kuroe, K. Ozawa, O. Suzuki, H. Kitazawa, G. Kido, and T. Sekine, Magnetic properties of $Rb_2Cu_2Mo_3O_{12}$ including a one-dimensional spin-1/2 Heisenberg system with ferromagnetic first-nearest-neighbor and antiferromagnetic Second-Nearest- Neighbor Exchange interactions, Phys. Rev. B **70**, 104426 (2004).

[46] S. Okubo, H. Wada, H. Ohta, T. Tomita, M. Fujisawa, T. Sakurai, E. Ohmichi, and H. Kikuchi, Anomalous spin dynamics observed by high-frequency ESR in honeycomb lattice antiferromagnet $InCu_{2/3}V_{1/3}O_3$, J. Phys. Soc. Jpn. **80**, 023705 (2011).

[47] T. Kubo and R. Toyabe, *Magnetic Resonance and Relaxation* (North-Holland, Amsterdam, 1996).

[48] J. Sugiyama, K. Mukai, H. Nozaki, M. Harada, M. Månsson, K. Kamazawa, D. Andreica, A. Amato, and A. D. Hillier, Antiferromagnetic spin structure and lithium ion diffusion in Li_2MnO_3 probed by μ^+SR, Phys. Rev. B **87**, 024409(R) (2013).

[49] H. Nozaki, J. Sugiyama, M. Månsson, M. Harada, V. Pomjakushin, V. Sikolenko, A. Cervellino, B. Roessli, and H. Sakurai, Incommensurate spin-density-wave order in quasi-one-dimensional metallic antiferromagnet NaV_2O_4, Phys. Rev. B **81**, 100410(R) (2010).

[50] R. S. Hayano, Y. J. Uemura, J. Imazato, N. Nishida, T. Yamazaki, and R. Kubo, Zero-and low-field spin relaxation studied by positive muons, Phys. Rev. B **20**, 850 (1979).

[51] J. Sugiyama, H. Nozaki, I. Umegaki, W. Higemoto, E. J. Ansaldo, J. H. Brewer, H. Sakurai, T.-H. Kao, H.-D. Yang, and M. Månsson, Hidden magnetic order in Sr_2VO_4 clarified with μ^+SR, Phys. Rev. B **89**, 020402(R) (2014).

[52] A. L. Hector, C. S. Knee, A. I. MacDonald, D. J. Price, and M. T. Weller, An unusual magnetic structure in Sr_2FeO_3F and magnetic structures of K_2NiF_4-Type Iron(III) oxides and oxide Halides, including the cobalt substituted series $Sr_2Fe_{1-x}Co_xO_3Cl$, J. Mater. Chem. **15**, 3093 (2005).

Correction: The middle initial of the fourteenth author was missing and has been fixed.